Supplementary Information (Data Repository [DR1])

1.1 Near-source Tephrostratigraphy and Tephra Correlations (Volcanic Glass chemistry)

The 87.5m long S-19 borehole (40.883 Lat; 14.251 Long; 93m altitude) was drilled ~ 5 km NE of the Campanian Ignimbrite (CI) caldera rim (**Fig. 1B**). The sequence preserves pyroclastic deposits of numerous eruptions, which are interlayered between palaeosols, peat, marine sediments, along with reworked continental deposits. The deposits of the Neapolitan Yellow Tuff (NTY) are found at 15.5 m below the ground surface, while the top of the CI was encountered at a depth of ~ 29.5 m. There are 6 primary tephra units in the 14 meter succession from the Tufi Biancastri (TB) sequence. The primary pyroclastic deposits vary in thickness from a few cm to more than 3 m. The thickest tephra is the third primary unit (3) above the CI deposit, it is 3.4 meters thick and spans 25.9 to 22.5 meters (Fig. 2). The basal part of this deposit is composed of 5 cm of well sorted, yellow/orange coloured fine ash, and overlying this is well-stratified, millimetre to centimetre thick stratifications of millimetre sized pumice fragments that are light grey in colour. This 5 cm sub-unit is separated from the overlying thicker portion of the deposit by a sharp planar contact. The upper sub-unit is a grey to light-grey, fine-medium to coarse ash deposit with abundant large (up to 2.5 cm in diameter) accretionary lapilli, and millimetre to a few centimetre-sized angular grey pumices that are porphyritic with biotite and pyroxene crystals and minor feldspar. Sometimes the pumice fragments are characterized by elongated vesicles, and occasionally the pumices are concentrated in thin levels. This upper sub-unit of Unit 3 (3.3 meters) in S-19 is interpreted as a pyroclastic density current (PDC) deposit.

Overlying the CI at the investigated Ponte Rossi (PR) outcrop (40.877 Lat; 14.265 Long; 60m altitude) were eight eruption units interbedded with paleosols, representing eruption hiatuses at the site, allowing periods of soil formation (Fig. S1). The fourth unit above the CI is the thickest in the PR succession, totalling 90 cm (Fig. S1). It rests on a thin, poorly developed paleosol (evidence of humification), which caps a 10 cm thick, poorly sorted fine- to coarse ash unit (Sample CF129). The basal 10 cm of PR eruption Unit 4 comprises well-stratified millimetre to centimetre sized, moderately sorted, fine to medium pumice lapilli fall with occasional lithics (sample CF131; Fig. S1). Following a sharp contact, there is 30 cm of moderately well-sorted fine ash that gradually transitions into 20 cm of poorly sorted ash and pumice lapilli, with pumice lapilli up to 7 cm in diameter. This unit also contains abundant accretionary lapilli with pumice fragments as cores, and are up to 2.5 cm in diameter. The upper portion of PR Unit 4 comprises of 30 cm of poorly sorted, fine to coarse ash (sample CF132), and this is interpreted as a PDC deposit.

The deposit characteristic of the post-CI S-19 Unit 3 and the PR Unit 4 show a large degree of similarity supporting their stratigraphic correlation. Indeed both these eruption units are the thickest deposits in their respective post-CI stratigraphic successions and contain large accretionary lapilli, which are not observed in any of the other Tufi Biancastri units.

Major and trace element volcanic glass chemistry were used to establish the stratigraphic correlations of tephra units in the Ponti Rossi (PR; SFig. 1) and S-19 borehole Tufi Biancastri (TB) sequences, and their correlation to the distal Y-3 tephrostratigraphic marker (Albert et al., 2015). Grain-specific glass chemical analysis was carried out on individual pumice and ash grains from the near-source deposits. Major and minor elements were determined using

a wavelength-dispersive JEOL 8600 electron micro-probe (EMP) at the University of Oxford, with an electron beam accelerating voltage of 15kV was used with a 6nA current with a beam diameter of 10 µm following the methods and data accuracies reported in Smith et al. (2011). Accuracies were monitored using reference glasses (ATHO-G, StHs6/80 and GOR132) from MPI-DING (Jochum et al., 2006) and are these analyses are provided in the **Data Repository 2**.

Trace element analysis was determined using laser ablation inductively coupled plasma mass spectrometry (LA-ICP-MS), with a Thermo Scientific iCAP Qc ICP-MS coupled to a Teledyne Photon Machines Analyte G2 193 nm eximer laser ablation system with a HelEx II two-volume ablation cell at Trinity College, Dublin. The trace element analyses were carried out using a 25 µm spot, the laser repetition rate was 5 Hz and the count time was 40 s (200 pulses) on the sample and 40 s on the gas blank (background). The ablated sample was transported in He gas flow (0.65 L min^{-1}) with additional N_2 (5 ml min^{-1}) via a signal smoothing device. Concentrations were calibrated using NIST612 with ^{29}Si as the internal standard, where EPMA data reveals mingled clasts/shards the appropriate ^{29}Si value was used by comparing the ^{44}Ca concentration measured using the LA-ICP-MS with those of the EPMA. Data reduction was performed using Iolite 2.5 and portions of the signal compromised by the ablation of microcrysts and resin-filled voids were excluded. Accuracies of reference glasses (ATHO-G and StHs6/80-G MPI-DING; Jochum et al., 2006) are typically ≤5% for all elements. Full glass chemical data sets for the Masseria del Monte Tuff (PR samples CF131/132 and S-19 (25.9-22.5m) are presented in **Data Repository 2**, along with secondary standards run alongside the unknown tephra deposits, and those from Albert et al., (2015).

Representative analyses of the PR (CF 131/132) and S-19 (25.8m/22.9m) tephra are provided here in **Table S1,** along with that of the type locality Y-3 tephra in the Ionian Sea. Tephra correlations were verified by a range of diagnostic major and trace element bi-plots as defined in Albert et al. (2015) (**Fig. S2**). The thin ash fall unit at PR underlying the Masseria del Monte Tuff/Y-3 eruption deposit, the third unit above the CI also contains the diagnostic bi-modal major element phono-trachytic and trachytic components (1 and 2) consistent with the distal Y-3 tephra, however trace element data indicate that this unit is characterised by higher levels of incompatible trace element enrichment, this in conjunction with its limited thickness allow us to exclude it as the near-source equivalent of the widespread Y-3 tephra (**Fig. S2**). The possibility that by combining the compositions of two eruption deposits, such as CF128, and CF129, to satisfy the overall compositional variability of the distal Y-3 tephra is not possible as they are separated by a well-developed palaesol, temporal hiatuses allowing such soil formation (hundreds to thousands of years) would have resulted in separate layers in some of the higher resolution sedimentary records of the Mediterranean region (e.g., Lago Grande di Monticchio).

1.2 Geochronology $^{40}Ar/^{39}Ar$ Geochronology (LSCE-BGC):

$^{40}Ar/^{39}Ar$ geochronology was performed on pristine sanidine crystals from three near-source pyroclastic samples, one sample was analysed at Laboratoire des Science du Climat et de l'Environment (CNRS-LSCE; Gif Su Yvette, France) and a further two samples were analysed at the Berkeley Geochronology Center (BGC; Berkeley, USA). Weighted mean ages of both the LSCE and BGC dates are calibrated to the age of the Alder Creek Sanidine

(ACs) =1.1891 ± 0.0008 Ma (1σ, Niespolo et al., 2017) and the decay constants of Renne et al (2011).

1.2.1 CNRS-LSCE

Sanidine crystals from tephra sample S-19-22.9m were sieved and washed in water. Clear and unaltered sanidine crystals ranging from 250 µm up to 1 mm in size were handpicked under a binocular microscope. To prevent any groundmass contamination, crystals were leached for 5 min in dilute (5 to 7%) hydrofluoric acid. Approximately 40 crystals were then chosen and loaded separately in aluminium disks in order to obtain ages on single-grains (N1530-01 to 17) or on small populations (2 to 3 crystals, N1539-01 to 07) when the grains were to small to be measured individually. Samples were then irradiated for 45 min (IRR 119, J value = 3,6070. 10-4) in the β1 tube of the OSIRIS reactor (French Atomic Energy Commission, Saclay, France). After irradiation, samples were transferred into a copper holder and crystals were loaded in individual holes. This copper holder was then placed into a differential vacuum Cleartran© window. Sanidines were then fused using a Synrad CO_2 laser (ca. 25 Watts) and the relative quantities of the argon isotopes (^{40}Ar, ^{39}Ar, ^{38}Ar, ^{37}Ar and ^{36}Ar) were measured using a VG 5400 mass spectrometer equipped with a single ion counter (Balzers SEV 217 SEN). Each Ar isotope measurement consisted of 20 cycles of peak switching of the argon isotopes. J values were obtained by co-irradiation of the Alder Creek sanidine standard (ACs-2 at 1.1891 ± 0.0008 Ma (1σ); Niespolo et al., 2017; Renne et al., 2011) placed in the same pit as the samples during irradiation. Mass discrimination was assessed by analysis of air pipette throughout the analytical period, and was calculated relative to a $^{40}Ar/^{36}Ar$ ratio of 298.56 (Lee et al., 2006). Procedural blanks were measured every two or three unknown measurements. For a typical 10 min static blank, the backgrounds were generally about 3.0–4.0 × 10^{-17} and 6.0–7.0 × 10^{-19} mol for ^{40}Ar and ^{36}Ar, respectively. The nucleogenic production ratios used to correct for reactor-produced Ar isotopes from K and Ca are reported in the **Data Repository 3**.

1.2.2 BGC

Sanidine from tephra samples S-19-25.8m and PR-CF132 were sieved and washed in distilled water in an ultrasonic bath. Sanidine grains were separated using a Frantz Isodynamic magnetic separator and heavy liquids. S-19 tephra sample 25.8 was rinsed in dilute HF for one minute. All samples were finally handpicked to purity. Sanidine crystals from S-19-25.8m and from PR-CF132 were loaded into a sixteen-pit 18.5-mm aluminium disk: samples were placed into large 4.5- mm diameter; Alder Creek sanidine (ACs) crystals were loaded into surrounding 3.18-mm pits as a neutron fluence monitor (Nomade et al., 2005). The disk was irradiated for 1 hour at the Cd-lined, in-core CLICIT facility of the Oregon State University TRIGA reactor and labelled irradiation 457PRA. J-values of samples were determined by interpolation of a planar fit to J-values determined from the ACs fluence monitor using the optimization age of 1.1891 ± 0.0008 Ma (1σ) (Niespolo et al., 2017; Renne et al., 2011).

Sanidine crystals from S-19-25.8 and PR-CF132, and ACs standards, were analysed on a MAP 215-50 mass spectrometer, dubbed Nexus, with a Nier-type ion source and an analogue electron multiplier detector. Single grains of the samples underwent total laser fusion from a CO_2 laser at 7 Watts of power. ACs samples from small pits were measured by total fusion of 3-grain aliquots. For each sample, blank and air pipette, fifteen cycles at 8-35

integrations per cycle were determined for each Ar isotope using peak hopping by magnetic field switching on a single detector. Evolved gases were cooled to ca. -130 to -135 ^{o}C using a cryotrap and exposed to a c. 450 ^{o}C hot getter to remove reactive gases. For all samples, a mean blank correction was determined using background isotopic measurements analysed between each single-grain analysis. Blanks between sample measurements were stationary over time, and mean values and standard deviations were used to correct the sample and air pipette data. Mass discrimination was determined based on automated analyses of air pipettes between every five single grain analyses (plus intercalated blanks) using air pipette data based on a power law correction (Renne et al., 2009) and the atmospheric values of Lee et al. (2006). See the **Data Repository 3** for mass discrimination values.

Ar isotopic measurements of sanidine crystals from PR-CF132 and ACs standards were also analysed on a *Noblesse* 5-collector sector-magnet mass spectrometer, configured with one axial Faraday detector and four off-axis, symmetrically arrayed ETP ion counters. Quasi-uniform heating of each sample (a single grain of sanidine) was achieved via illumination with a CO_2 laser fitted with a beam-shaping lens to generate a flat energy profile of adjustable diameter, typically 2 mm at the target distance. Individual grains of ACs sanidine were heated for ~30 seconds at progressively increasing power levels (1.5–8 watts) until fusion was achieved, typically in 3-4 steps. Evolved gas was exposed for several minutes to an approximately -130°C cryotrap to remove H_2O, and to a GP-50 SAES getter to remove reactive gases. Integrated ages of the step-heating results of ACs were used to calculate J values and provide the basis for liner interpolation of J values for unknowns. Single grains of CF132 were totally fused at 8-9 watts. Five Ar isotopes were measured, with simultaneous measurement of ^{40}Ar, ^{37}Ar, and ^{36}Ar on separate ion counters over a period of ~800 seconds, alternating with peak hopping to position ^{38}Ar and ^{39}Ar on the same ion counter as ^{40}Ar. All signals were normalized to the ^{40}Ar ion counter. ^{36}Ar signal normalization was achieved through periodic measurement of the ^{40}Ar/^{36}Ar ratio of air argon (Lee et al., 2006) inlet from an air-reservoir pipetting system. ^{37}Ar and ^{38}Ar signal normalizations were achieved through periodic measurement of ^{40}Ar from a static gas sample on relevant detectors in a round-robin peak-hopping procedure. Procedural blanks, matching sample gas extractions precisely but without firing the laser, were run every four analyses. The Noblesse instrument has sufficiently high resolution to distinguish an almost entirely hydrocarbon free shoulder at mass 36, where the measurement for ^{36}Ar is made. For further details of the analytical procedures refer to Deino et al. (2010). Interference corrections for all data are after Renne et al. (2015) and are included in the **Data Repository 3**.

1.2.3 Integrating the ^{40}Ar/^{39}Ar data

^{40}Ar/^{39}Ar ages, including *R*-values are presented in **Table S3**. Individual probability diagrams are presented below in **Figures S3-6**. The overall rank order of all analyses used in generated the fully integrated ^{40}Ar/^{39}Ar weighted mean age for the eruption deposit at Campi Flegrei Caldera are presented in **Figure S7**. All measurements are provided in **Data Repository 3**.

S-19 25.9-22.5 m (3rd eruption deposit above the Campanian Ignimbrite in S-19 borehole)

A total of twenty-four ^{40}Ar/^{39}Ar measurements for the S-19 sample 22.9 were made at LSCE. The first seventeenth measures were obtained by the analyses on single grains while the last seven others were done by the analyses of small crystal populations (two or three

crystals simultaneously fused). The results obtained present a clear bi-modal probability diagram (**Fig. S3**) with two distinct populations. Both populations are homogeneous, with the dominant younger population comprising eighteen of the twenty-four measurements made. The $^{40}Ar/^{39}Ar$ weighted mean age determined for this upper portion of the eruption deposit is 29.0 ± 0.8 ka (2σ). A secondary population of ages cluster at ~40 ka, consistent with the age of the large CI eruption (Giaccio et al., 2017), confirming them as a population of xenocrysts. The 2 sigma age range of the CI xenocrysts identified in the S-19 22.9 m sample can be used, in conjunction with the stratigraphic position of all investigated units above the CI, as a basis to exclude CI xenocrysts from the remaining samples analysed. If the uncertainties of individual analyses have been properly quantified and the tephra has been adequately sampled, we expect a single population of data representing one event to yield MSWD = 1. Uncertainties increase if gas yields are low and the blank correction becomes significant compared to the gas measurement, as is expected with young samples and/or smaller grain sizes. Removing the CI-age grains yields MSWD < 1 for each BGC data set due to 1σ uncertainties of individual analyses ranging from ~1-10 ka, but removal also results in probability (P) ~ 1 and the results agree with geologic/stratigraphic information necessitating the exclusion of those grains. Fifty-nine sanidine crystals from the S-19 borehole sample 25.8 m (post-CI ERU3) analysed at BGC (Nexus), fifty-seven of which present a unimodal probability distribution (**Fig. S4**). However, considering the higher precision dating of the upper portion of eruption deposit (Sample 22.9 m), thirteen of the fifty-seven crystals can be interpreted as CI xenocrysts and removed from the age computation. The $^{40}Ar/^{39}Ar$ weighted mean age for the basal portion of the post-CI ERU3 in the S-19 core is 28.4 ± 2.1 ka (2σ) (MSWD = 0.52, P=1, n=44). The combined $^{40}Ar/^{39}Ar$ weighted mean age for the S-19 25.9-22.5 m eruption deposit is 29.0 ± 0.8 ka (2σ).

Ponti Rossi- CF132 age (4th eruption deposit above the Campanian Ignimbrite at Ponti Rosi)

Two independent ages were produced for the upper portion of PR eruption deposit (sample CF132). Thirty-two sanidine crystals were analysed at BGC using Nexus instrument, thirty-one of which present a uni-modal probability distribution (**Fig. S5**). Eight of thirty-one crystals were removed based on our stratigraphic and geochemical correlations of this eruption deposit to the more precisely dated tephra in the S-19 borehole (sample 22.9 m) which clearly resolves the CI xenocrystic material. The $^{40}Ar/^{39}Ar$ weighted mean age of the PR-CF132 sample using Nexus is 31.6 ± 2.8 ka (MSWD = 0.33, P =1, n= 23). Eighteen sanidine crystals analysed at BGC using the Noblesse instrument, fifteen of which present a uni-modal density distribution (**Fig. S6**). Four of the fifteen crystals were removed as CI xenocryst as for reasons previously outlined for the Nexus analysis of the sample. The $^{40}Ar/^{39}Ar$ weighted mean age of the PR-CF132 sample using Noblesse is 31.3 ± 2.6 ka (MSWD = 0.15, P = 1.0, n = 11), indistinguishable from the results produced using Nexus. The combined $^{40}Ar/^{39}Ar$ weighted mean age for the CF132 is 31.4 ± 1.9 ka (2σ).

Integrated CFc near-source ($^{40}Ar/^{39}Ar$) geochronology

The $^{40}Ar/^{39}Ar$ weighted mean age of the PR-CF131/132 (31.4 ± 1.9 ka) and of S-19 (29.0 ± 0.8 ka) eruption deposits are statistically indistinguishable at the 95.4% confidence limit, even if their respective uncertainties differ largely in magnitude (**Table S3**). This is due to the difference in how each laboratory imposes blank corrections on the samples. CNRS-LSCE applies a bracketing blank correction which imposes the analytical uncertainty only from the blanks run before and after the unknown analysis, while BGC imposes a mean blank

correction with a standard deviation from many (or all) blanks run over the course of the total number of analyses of a sample. The latter approach is a more conservative application of a blank correction in that it captures the variability among the blanks themselves, resulting in a larger error contribution from the blank correction imposed on the unknown and a larger uncertainty on the final age of a sample. The overall agreement in age, coupled with the robust stratigraphic and geochemical correlation, allow us to combine the ages of the near-source units (PR-CF131-132 and S-19 25.9-22.5m). The combined rank-order distribution of all the analysed grains used from CNRS-LSCE and BGC to generate the $^{40}Ar/^{39}Ar$ weighted mean age of the eruption are presented in S. Figure 6. The $^{40}Ar/^{39}Ar$ weighted mean age for this eruption at CFc of 29.34 ± 0.71 ka (2.σ).

1.3 Ash dispersal modelling

Ash dispersal associated with the Y-3 tephra deposits originating from CFc were simulated using the HAZMAP model, which solves equations for advection, diffusion and sedimentation of particles in two dimensions (Macedonio et al., 2005). This model assumes that atmospheric dispersion of particles through wind transport and effective turbulent diffusion, with fallout being controlled by terminal settling velocity (Macedonio et al., 2005). Isopach maps were generated by modelling the tephra deposition in terms of mass loading (kg m^{-2}) and converting to thicknesses, using a bulk density of 1000 kg m^{-3}, similar to other Campanian eruption deposits (Costa et al., 2009).

Input parameters required for the dispersal model include: total erupted mass, eruption column height, mass distribution along the column, total grain-size distribution (TGSD), wind profile, and effective horizontal diffusion coefficient. As there is no direct way to estimate all these parameters pertaining to the time of the eruptions, they were reconstructed by best fitting observations of tephra thickness through minimizing the difference between observed and modelled thickness (Costa et al., 2009; Matthews et al., 2012) using the equation:

$$s^2 = \sum_{i=1}^{N} w_i \left[T_i(obs) - T_i(calc) \right]^2 \quad \text{(S.1)}$$

Where N is the number of data points (sample localities), w_i is the weighting factor, and $T_i(obs)$ and $T_i(calc)$ represent the observed and calculated thicknesses, respectively. Weighting factors depend on the distribution of random errors in the dependant variable. All values have the same weight when w_i =1 is used, and when $w_i = 1/T^2_i$ (obs) is used the relative squared errors are minimised (i.e., proportional weighting). The use of $w_i = 1/T_i(obs)$ is a compromise between the minimising absolute and relative squared errors. In addition to the above equation, as in Costa et al. (2014) and Poret et al. (2017), we computed the statistical indexes K (i.e. geometric average of the distribution) and k (i.e. geometric standard deviation of the distribution) that were introduced by Aida (1978) (see **Table S4**):

$$K = exp\left[\frac{1}{N}\sum_i^N \log\left(\frac{T_i(obs)}{T_i(calc)}\right)\right]; \quad k = exp\left[\sqrt{\frac{1}{N}\sum_i^N \log\left(\frac{T_i(obs)}{T_i(calc)}\right)^2 - \left(\frac{1}{N}\sum_i^N \log\left(\frac{T_i(obs)}{T_i(calc)}\right)\right)^2}\right] \quad \text{(S.2)}$$

In the model, the total erupted mass was calculated analytically to minimise the difference between the modelled and observed layer thicknesses, optimizing either the relative error (S.1) (proportional weighting) or the Aida indices (S.2). The column height was assessed in the range of 30-60 km and was trailed in 1 km steps. The model assumes deposition was

from a filiform eruption column extending from a source area within CFc and an effective average wind field across the region. The other parameters and the explored ranges are reported in **Table S4**. There were six granulometric size classes assumed in the eruption source parameters, with five representing particles falling as single particles and, following Cornell et al. (1983), the last representing aggregates formed of fine particles (or single particles having an equivalent settling velocity). Owing to a lack of available grain size information to allow the TGSD to be reconstructed, we adopted information from the well-studied deposits of the Campanian Ignimbrite eruption (**Table S5**, Marti et al., 2016). With respect to the parameterization proposed by Cornell et al. (1983), which accounts for the effects of ash aggregation, we assumed that all particles smaller or equal to 62 microns fall as aggregates class with diameters of 200 microns (as in Cornell et al., 1983) (**Table S6**). The Y-3 tephra is found but relatively confined, which suggests efficient aggregation and supports the assumption that the small particles (62 microns) fell as aggregates.

It is important noting that the diverse eruption source parameter combinations and the inter-dependency of input parameters used in the tephra dispersal model means the best-fit solution is not unique (e.g., Bonasia et al., 2010; Connor & Connor, 2006; Marti et al., 2016). Furthermore, the lack of detailed granulometry data to reconstruct the TGSD for the deposits introduces large uncertainties. However, our sensitivity tests indicate that the total erupted mass is in the range of 10-30 km^3 DRE and the plume height was between 40 and 60 km. For a more information on the approach employed to model the tephra dispersal and its limitations refer to Costa et al. (2009) and Matthews et al. (2012).

Table S1: Localities of Masseria del Monte Tuff and distal Y-3 tephra fall deposit thicknesses incorporated into the HAZMAP ash dispersal model. Proximal and medial (SMP1e) PDC unit thicknesses are incorporated in the volume estimate using the methods of Macedonio and Pareschi (1991). *At PR 10 cm of moderately-sorted pumice lapilli fall and 30 cm of ash fall. **In S-19, 5 cm moderately-sorted pumice fall lapilli fall and 5 cm of ash fall. ***active marine canyon, assumed to be flow deposits. ****Thickness for the simulations was assumed equal to 1 mm. ^Layer thickness not available. Also listed are distal visible and cryptotephra occurrences of the NYT used in Figure 1.

Site	Sequence (tephra)	Latitude	Longitude	Thickness (cm)		Reference
Masseria del Monte /Y-3 tephra				**Fall**	**PDC**	
Ponti Rossi (PR)	CF131-132	40.877	14.265	40*	50	This study
S-19 Borehole (Naples)	25.9-22.5m	40.883	14.251	10**	330	This study
Sorrentine Peninsula	SMP1-e	40.686	14.465	-	45	Sulpizio et al.,2003; Zanchetta et al., 2008
Sorrentine Peninsula	SMP1-e	40.768	14.654	-	100	Di Vito et al., 2008; Zanchetta et al., 2008
Lago Grande di Monticchio	TM-15	40.931	15.604	28.6	-	Wulf et al., 2004
San Gregorio Magno Basin	S-19	40.655	15.423	15	-	Munno and Petrosino, 2007
Lake Ohrid (OH-DP)	OH-DP-115	41.051	20.718	1.5	-	Leicher et al., 2015
Lake Ohrid (Co1202)	OT0702-4	41.088	20.78	3	-	Vogel et al., 2010
Lake Ohrid (Lz1120)	896-897	40.938	20.758	1	-	Wagner et al., 2008
Lake Ohrid (Jo-2004)	Jo-187	40.92	20.699	3	-	Caron et al., 2010
Lake Prespa (Co1215)	PT0915-05	40.993	20.995	1	-	Damaschke et al., 2013
Tenaghi Philippon (Greece)	TP2005 9.70m	40.968	24.25	Cryptotephra****	-	Albert et al., 2015; Wulf et al., 2018
Tyrrhenian Sea (KET-80-11)	205cm (C-7)	39.406	15.072	1	-	Paterne et al., 1988
Tyrrhenian Sea (KET-80-04)***	264-274 (C-7)	39.828	13.875	-	10***	Paterne et al., 1988
Adriatic Sea (MD90-917)^	920-17	41.17	17.37	-	-	Zanchetta et al., 2008
Tyrrhenian Sea (Core_C-106)	565-579cm	40.463	14.738	14	-	Munno and Petrosino, 2004
Ionian Sea	RC9-191(245-244) (Y-3)	38.249	17.993	1	-	Keller et al., 1978
Ionian Sea	M25/4-12(245-244) (Y-3)	37.964	18.274	1	-	Kraml, 1997; Albert et al., 2015
Ionian Sea	M25/4-13 (Y-3)	37.496	17.667	1		Kraml, 1997; Albert et al., 2015
Distal Neapolitan Yellow Tuff						
PAL94-77 (+others)	550	42.25	15.05	-	-	Calanchi et al., 1998
CM92-42	200	42.37	15.12	-	-	Calanchi et al., 1998
RF95-12	560			-	-	Calanchi et al., 2008
IN68-9	225			-	-	Calanchi et al., 2008

Lake Fucino	TF-2	41.98	13.55	3	-	Giaccio et al., 2017
Lago Grande di Monticchio	TM-8	40.931	15.604	2.2	-	Wulf et al., 2004
San Gregorio Magno Basin	S-19	40.655	15.423	80	-	Munno and Petrosino, 2007
Adriatic Sea (MD90-917)	395	41.17	17.378	-	-	Siani et al., 2004
Adriatic Sea (KET-80-22)	155	41.44	17.37	-	-	Paterne et al., 1988
Tyrrhenian Sea (KET-80-04)***	115 cm (C-2)	39.828	13.875	-	-	Paterne et al., 1988
Lake Bled (Slovenia)	Bld_T240	46.36	14.09	cryptotephra	-	Lane et al., 2011
Adriatic Sea (PRAD1-2)	PRAD-218	42.40	14.46	cryptotephra	-	Bourne et al., 2010
Langsee (Austria)	369.5	46.78	14.43	cryptotephra	-	Schmidt et al., 2002

Table S2: Representative major and trace element volcanic glass analyses of near-source eruptive products form the S-19 borehole (25.9-22.5m) and the Ponti Rossi outcrop (CF131/132) considered here equivalent to the distal Y-3 Mediterranean Tephrostratigraphic marker. Also given are representative average data from the two dominant glass populations of the Y-3 tephra from its type locality in the Ionian Sea (Albert et al., 2015).

Sample	S-19						Ponti Rossi					Y-3 Ionian Sea			
Core/Locality	S-19-25.8m			S-19-22.9m			CF131			CF132		(M25/4-12; Albert et al., 2015)			
Sample I.D	29D	19C	14B	14B	24C	9B	22D	13C	1A	4A		Average	(2 s.d)	Average	(2 s.d)
Component	1	2	3	1	2	mixing	1	3	mixing	1	2	1		2	
Major, minor												(n=12)		(n=17)	
SiO_2	62.45	60.46	59.75	62.05	60.70	61.92	62.67	60.98	61.18	62.27	60.41	62.41	0.65	60.58	0.53
TiO_2	0.44	0.37	0.50	0.30	0.42	0.31	0.38	0.43	0.37	0.41	0.36	0.37	0.08	0.38	0.05
Al_2O_3	18.26	18.68	18.45	18.16	18.73	18.25	18.02	18.06	18.28	18.14	18.60	17.97	0.32	18.42	0.20
FeOt	2.82	3.54	3.72	2.95	3.29	3.02	2.66	3.43	3.34	2.83	3.60	2.86	0.18	3.53	0.34
MnO	0.14	0.06	0.13	0.15	0.07	0.15	0.12	0.11	0.20	0.13	0.10	0.14	0.07	0.10	0.11
MgO	0.41	0.77	0.98	0.32	0.63	0.49	0.39	0.85	0.57	0.37	0.76	0.40	0.10	0.78	0.11
CaO	2.11	2.53	3.29	2.14	2.46	2.26	1.93	2.92	2.36	2.11	2.65	2.14	0.18	2.64	0.24
Na_2O	4.13	2.88	4.12	4.48	3.15	3.91	4.66	4.02	3.78	4.26	2.64	4.39	0.42	3.12	0.28
K_2O	8.40	10.10	7.99	8.42	9.93	8.96	8.31	8.20	9.14	8.62	10.33	8.54	0.35	9.96	0.28
P_2O_5	0.04	0.18	0.22	0.07	0.15	0.04	0.06	0.18	0.13	0.05	0.17	0.07	0.05	0.14	0.04
Cl	0.81	0.43	0.86	0.97	0.47	0.68	0.82	0.82	0.63	0.82	0.39	0.72	0.11	0.35	0.07
Analytical Total	96.35	95.71	98.41	96.68	97.34	94.90	94.54	98.21	98.17	94.66	95.14	95.90		96.68	
Trace															
Rb	330	297	344	329	256	310	351	333	327	364	280	345	*10*	273	10
Sr	130	534	369	181	463	269	116	330	281	139	574	137	11	558	106
Y	32	20	28	30	19	24	30	29	24	32	19	31	2	20	2
Zr	380	182	326	357	181	277	370	336	273	395	173	368	23	190	32
Nb	61	31	49	52	29	44	59	57	48	60	30	54	3	31	7
Ba	22	647	340	58	568	137	18	314	172	25	830	26	8	703	194
La	72	46	66	72	43	57	73	69	60	78	46	69	3	45	4
Ce	152	91	123	133	85	110	140	131	107	153	82	133	5	86	11
Pr	14.4	9.7	13.6	14.6	9.1	11.0	13.7	14.5	11.1	15.1	9.3	13.6	0.8	9.1	1.2
Nd	49.7	32.7	44.8	47.2	32.4	39.4	47.6	50.2	39.6	51.2	31.6	49.7	4.7	34.4	4.9
Sm	9.4	6.5	9.0	9.4	5.9	7.6	8.5	9.4	7.4	9.3	5.8	8.9	1.3	6.2	1.6
Eu	1.8	2.0	1.7	-	1.9	1.9	1.6	1.7	1.6	1.6	1.9	1.6	0.2	1.9	0.4
Gd	6.8	4.9	6.9	7.3	4.5	5.7	6.8	6.4	5.7	7.4	4.0	6.7	1.7	4.9	0.7
Dy	6.0	3.9	5.3	5.4	3.9	4.2	5.6	5.7	4.9	6.0	3.9	5.7	0.6	4.1	0.9
Er	3.0	2.0	2.9	3.4	1.8	2.4	3.0	3.2	2.3	3.2	1.8	3.1	0.2	2.0	0.4
Yb	3.4	1.9	2.5	2.8	1.9	-	3.4	-	-	3.4	-	3.1	0.4	1.8	0.4
Ta	2.7	1.4	2.4	2.8	1.3	2.1	2.7	2.8	2.1	2.9	1.3	2.8	0.3	1.5	0.4
Th	33.1	15.5	29.8	31.4	14.3	24.6	31.6	29.9	23.5	32.9	13.4	30.9	2.4	14.5	2.3
U	11.6	5.0	10.6	11.0	5.3	9.3	11.7	10.6	9.1	11.6	4.6	10.2	0.9	4.9	1.1
Nb/Th	1.8	2.0	1.6	1.7	2.0	1.8	1.9	1.9	2.0	1.8	2.3	1.8	0.1	2.1	0.2
Zr/Th	11.5	11.8	10.9	11.4	12.7	11.3	11.7	11.2	11.6	12.0	12.9	11.9	0.5	13.1	0.6
Nb/Zr	0.16	0.17	0.15	0.15	0.16	0.16	0.16	0.17	0.18	0.15	0.17	0.15	0.01	0.16	0.02

Table S3: Calculated $^{40}Ar/^{39}Ar$ ages and R-values for Tufi Biancastri deposits at Ponti Rossi (PR) sample CF-132, and S-19 borehole samples 25.8 and 22.9 m considered the near-source counterpart of the Y-3 tephra. Integrated $^{40}Ar/^{39}Ar$ weighted mean eruption age. Ages calculated with the air correction after Lee et al (2006), the ACs fluence monitor age of 1.1891 Ma (Niespolo et al., 2017) and the decay constants of Renne et al. (2011).

Sample	Mass Spec	Lab ID	R^{Y-3}_{ACs}	± (1σ)	R^{Y-3}_{FCs}	± (1σ)	Age, ka	± (2σ), ka	n/N
PR - CF 132	Noblesse	37163	0.026279	0.001107	0.001096	4.623E-05	31.25	2.64	11 / 18
PR - CF 132	Nexus	37163	0.026568	0.001156	0.001108	4.8286E-05	31.60	2.75	23 / 32
Core S19 - 25.8m	Nexus	37157	0.023888	0.000866	0.000996	3.6179E-05	28.41	2.06	44 / 63
Core S19 - 22.9m	VG 5400	N1530/ N1539	0.024464	0.000337	0.001020	1.4045E-05	29.00	0.80	18 / 24
Y-3 tephra - weighted mean			**0.024659**	**0.000292**	**0.001028**	**1.22E-05**	**29.34**	**0.71**	**96 / 137**

Table S4: Results of the HAZMAP tephra dispersal modelling of the Y-3 tephra from CFc. The values in brackets are the steps used in the model to assess the best-fit scenario.

Modelled dispersal parameters	**Explored range (step)**	**Y-3 tephra**
Fallout volume (DRE; km^3)	Calculated	16
Fallout mass (kg)	Calculated	4.5×10^{13}
Wind velocity (m/s)	1 to 50 (1)	12
Wind azimuth (o clockwise from North)	0 to 360 (1)	348
Column Height (H, km)	30 to 60 (1)	59
Suzuki Coefficient	1 to 9 (1)	7
Diffusion coefficient (K, m^2/s)	5000 to 80,000 (5000)	70,000
Deposit Density	Assumed to be similar to CI (1000)	
TGSD	Assumed to be similar to CI co-ignimbrite phase (Marti et al., 2016), with all particles </= 62 μm in diameter settling as aggregates with diameters of 200 μm.	

Table S5. TGSD of the co-ignimbrite/co-PDC phase of the Campanian Ignimbrite (Marti et al., 2016).

Φ	**%**
-1	0.37
0	1.45
1	1.80
2	3.05
3	8.50
4	17.90
5	24.17
6	20.77
7	12.66
8	6.36
9	2.28
10	0.68

Table S6. Effective TGSD used in the simulations. The aggregate density was estimated by the model, which explored a range of values (100 to 1500 kg/m^3). Particle terminal settling velocities were calculated according to Ganser (1993).

Particle diameter (Φ)	**Particle density (kg/m^3)**	**Particle sphericity (-)**	**%**
-1	500	0.85	0.37
0	725	0.85	1.45
1	950	0.85	1.80
2	1175	0.85	3.05
3	1400	0.85	8.50
Aggregate: Φ=2.3 (200 μm)	1000	1.00	84.83

Table S7. Observed vs simulated deposit thicknesses at the different locations.

Locations	Observed deposit (cm)	Simulated deposit (cm) from best *K* and *k* values	Simulated deposit (cm) from best σ^2 value
Ponti R_	40	24.55	19.09
S-19	10	24.05	18.70
Tenaghi Philippon	0.1	0.11	0.08
LGdM	28.6	31.08	24.17
OH-DP-	1.5	1.80	1.40
Co1202	3	1.59	1.24
Lz1120	1	2.05	1.59
JO-200	3	2.20	1.71
PT0915	1	1.61	1.26
SGMB	15	38.06	29.59
Core_C	14	25.18	19.58
KET_80	1	1.69	1.32
M25-12	1	0.44	0.35
M25-13	1	0.04	0.03
RC9-19	1	1.40	1.09
Statistical indices		*K* = 1.04; *k* = 2.67	σ^2 = 0.31

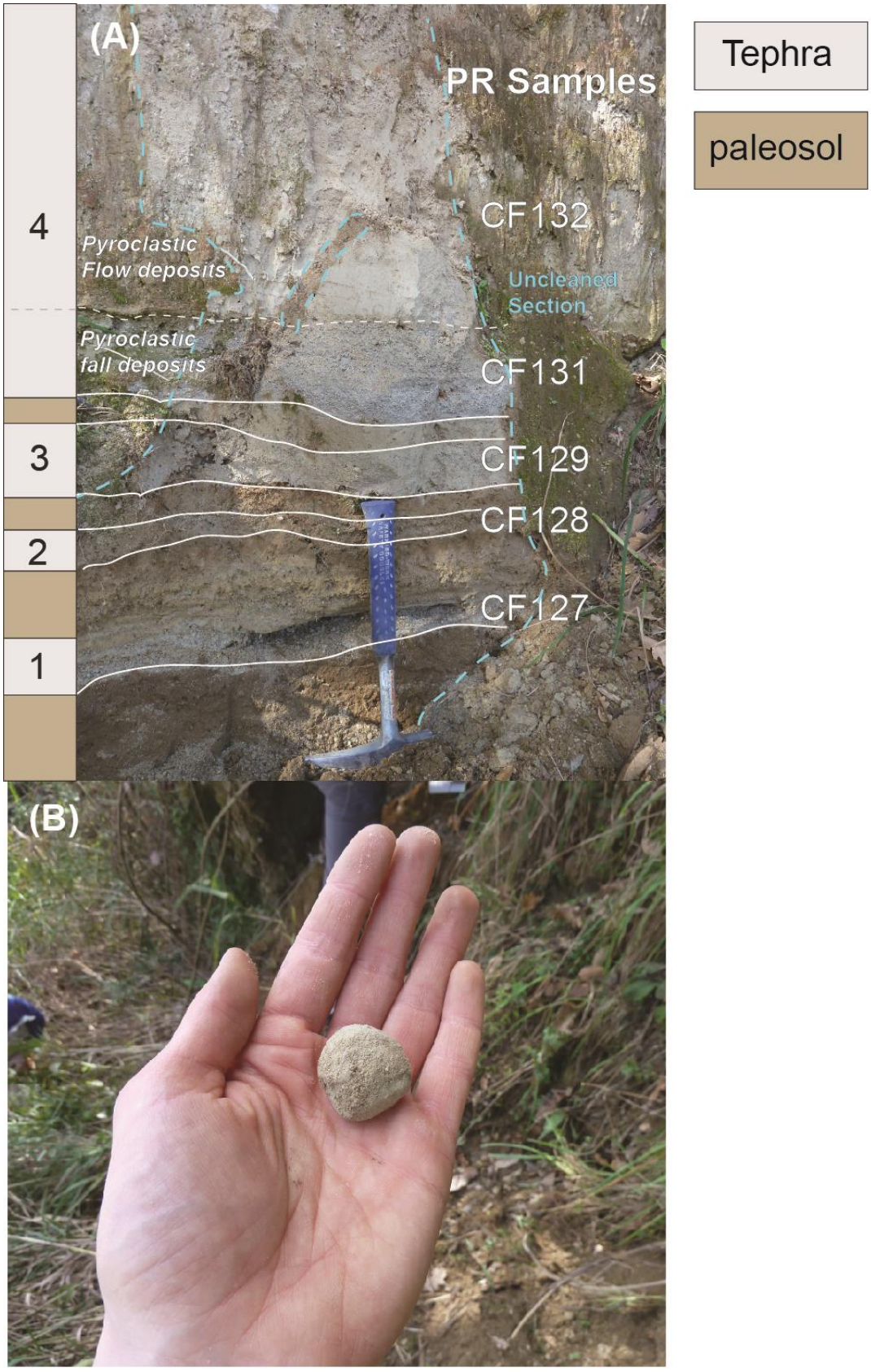

Figure S1: (A) The Ponti Rossi succession comprising of alternating tephra units and palaeosols, the thickest TB unit (fourth unit; CF131-132), has (B) large accretionary lapilli in the upper PDC deposits (sample CF132) and is correlated to the thickest unit in the S-19 borehole, which are both in turned correlated to the distal Y-3 tephra.

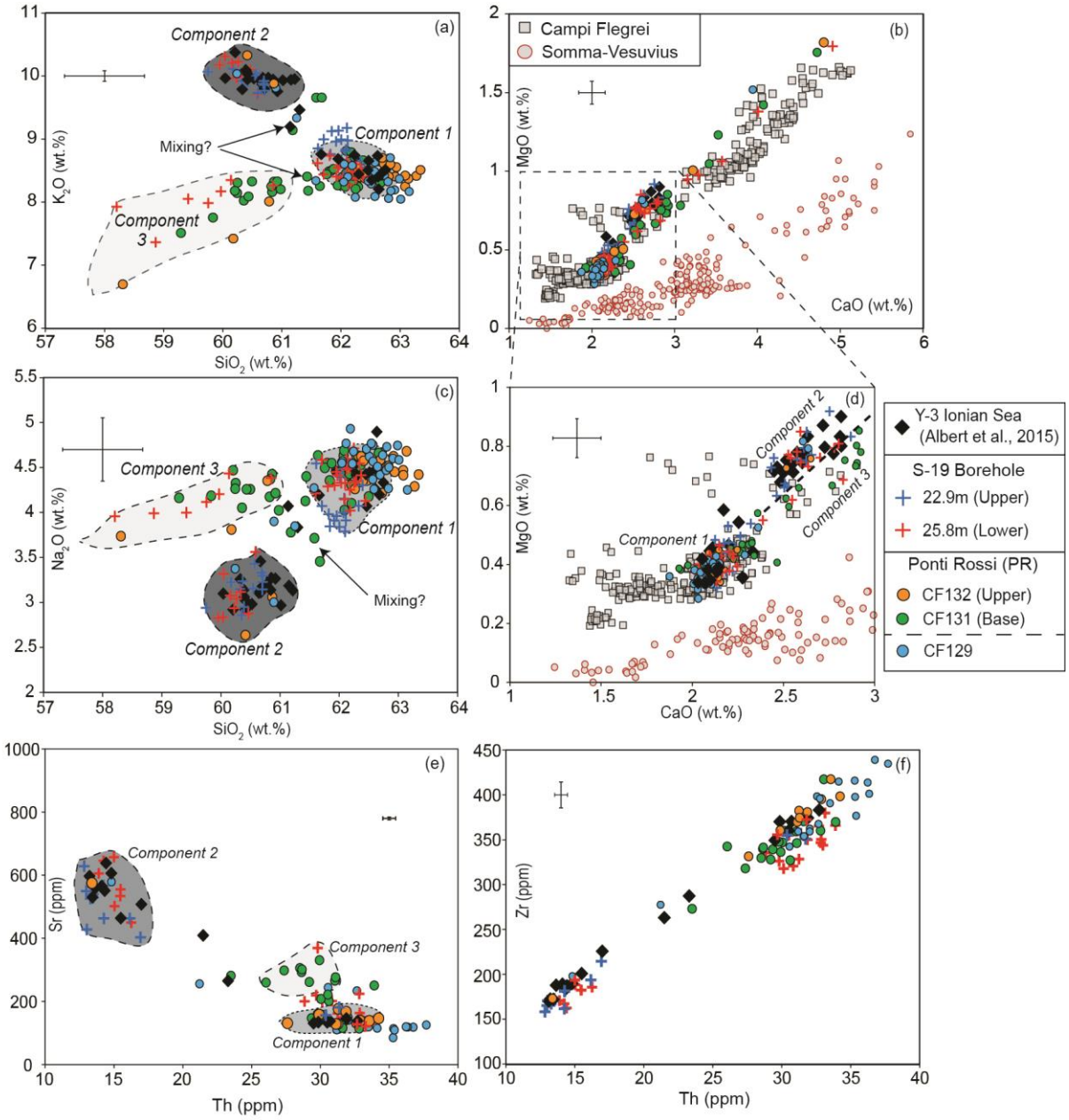

Figure S2: Selected major and trace element bi-plots illustrating the chemical correlation between the volcanic glasses of the Y-3 and the Ponti Rossi tephra (CF131/132) and borehole tephra (S-19 25.9-22.5m). (a-d) These bi-plots highlight the three compositional groupings referred to in the text. (e-f) highlight that the thin ash unit (CF129) at PR underlying the thickest tephra (CF131/132) extend to more elevated level of enrichment in incompatible trace elements than those observed in the distal Y-3 tephra.

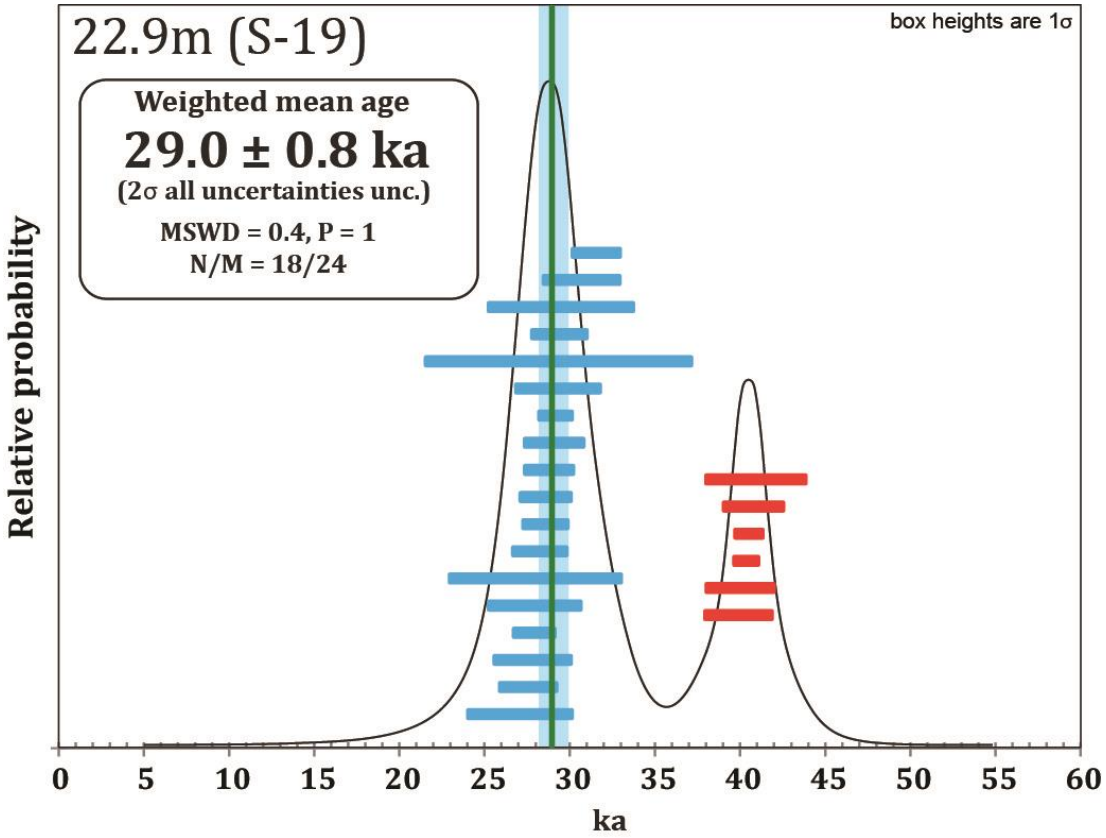

Figure S3: Bi-modal probability of the sample S19-22.9m sample analysed at LSCE and its $^{40}Ar/^{39}Ar$ weighted mean age. Age generated excludes the 40 ka CI xenocrysts population (red; see text)

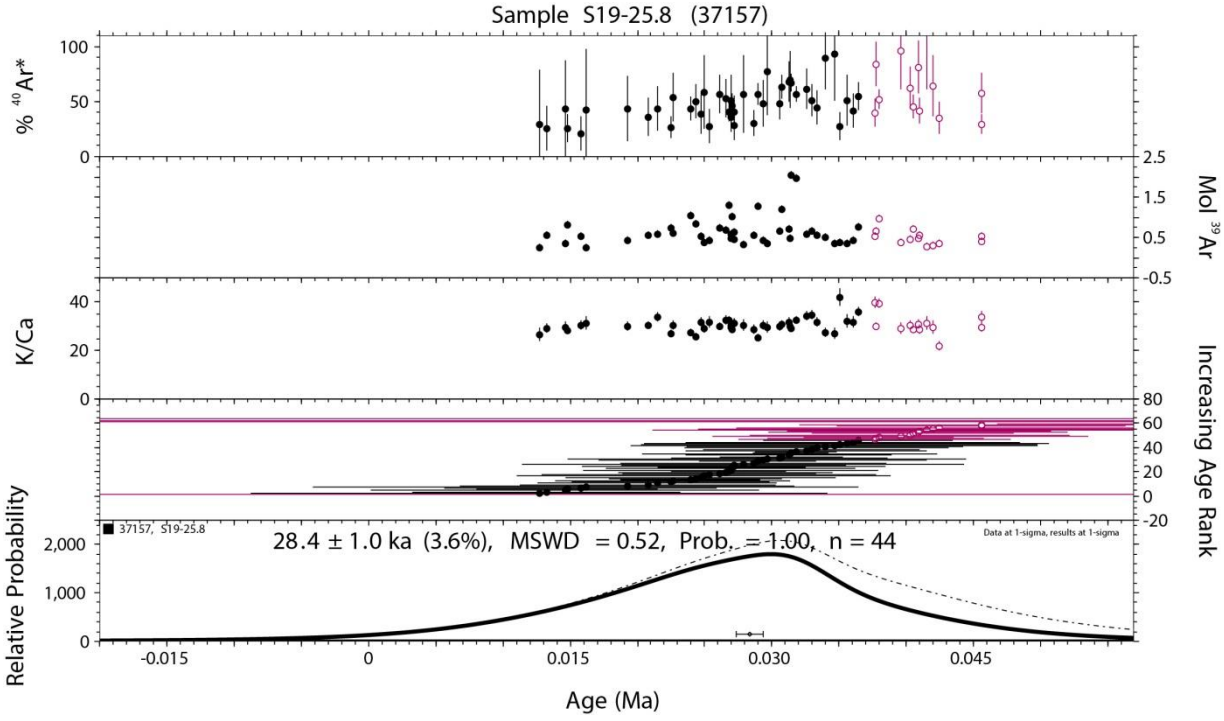

Figure S4: Unimodal probability distribution of sample S-19 25.8m and $^{40}Ar/^{39}Ar$ weighted mean age for sample S19-22.9m sample analysed using Nexus at BGC. Pink analyses were removed as CI xenocrysts (See text above).

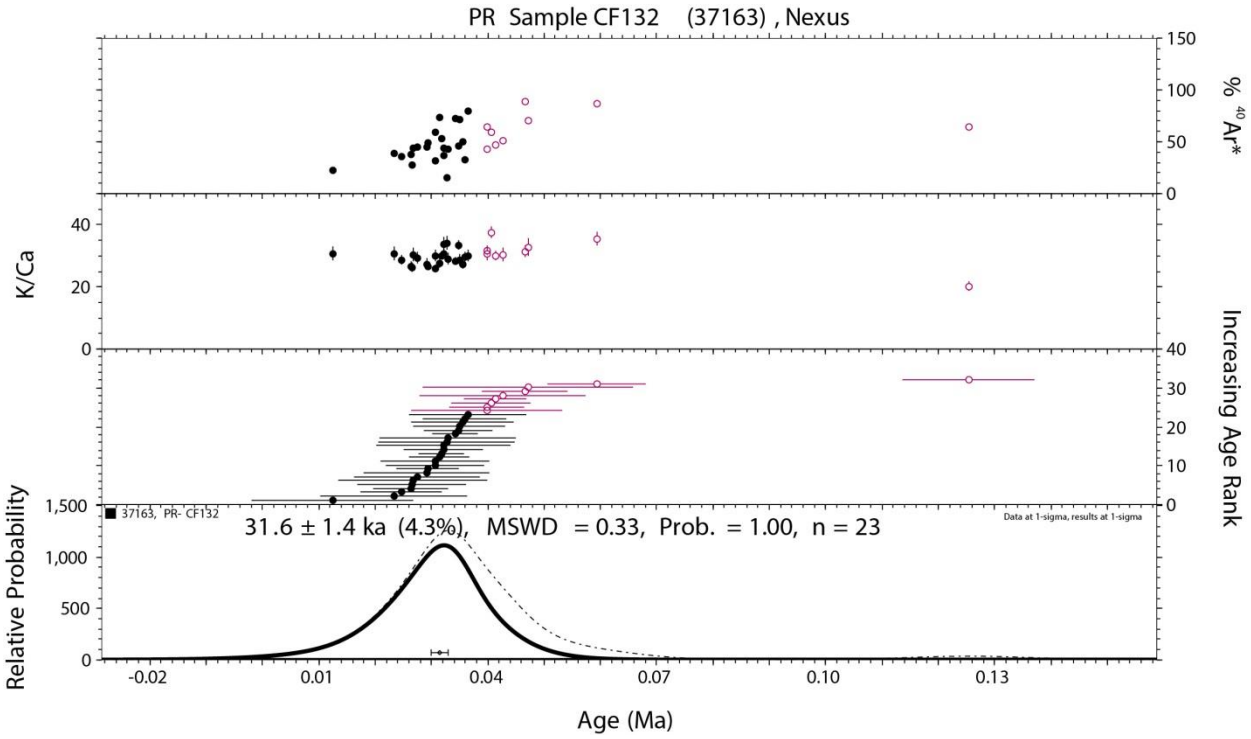

Figure S5: Unimodal probability distribution of sample S-19 25.8m and $^{40}Ar/^{39}Ar$ weighted mean age for the PR sample CF132 sample analysed using Nexus at BGC. Pink analyses were removed as CI xenocrysts (See text above).

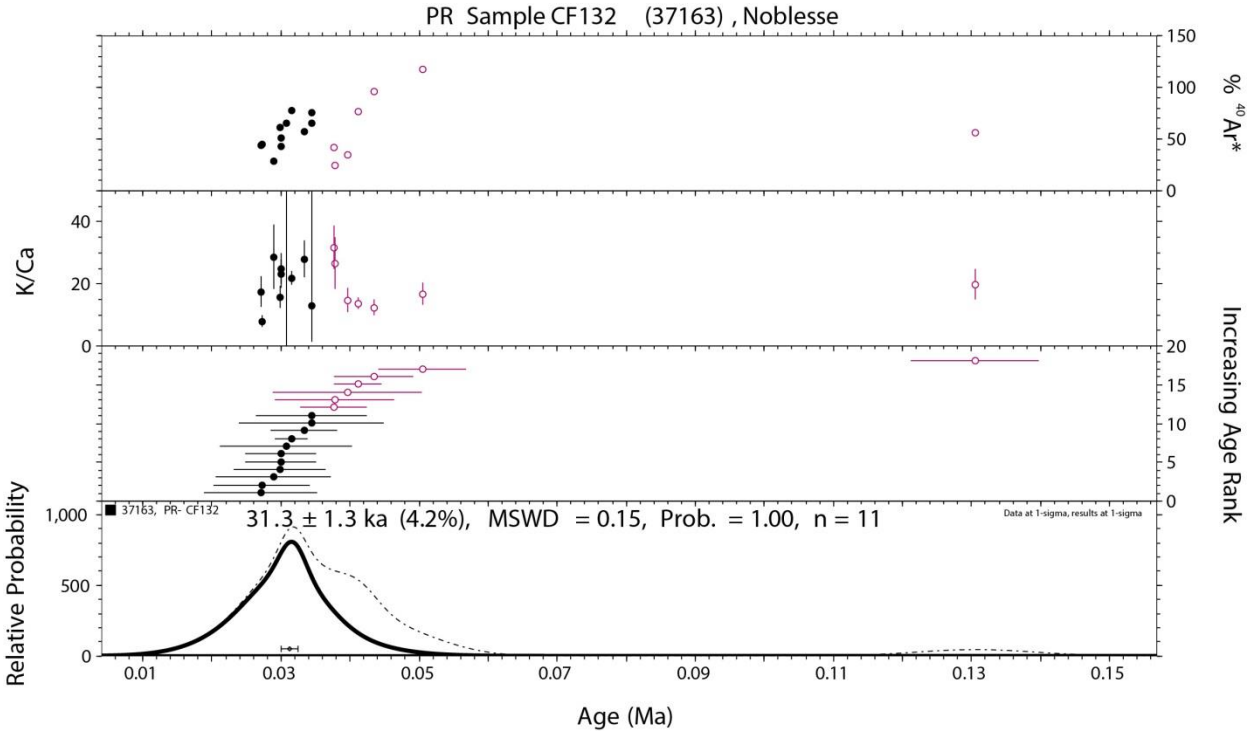

Figure S6: Unimodal probability distribution of sample S-19 25.8m and $^{40}Ar/^{39}Ar$ weighted mean age for the PR sample CF132 sample analysed using Noblesse at BGC. Pink analyses were removed as CI xenocrysts (See text above).

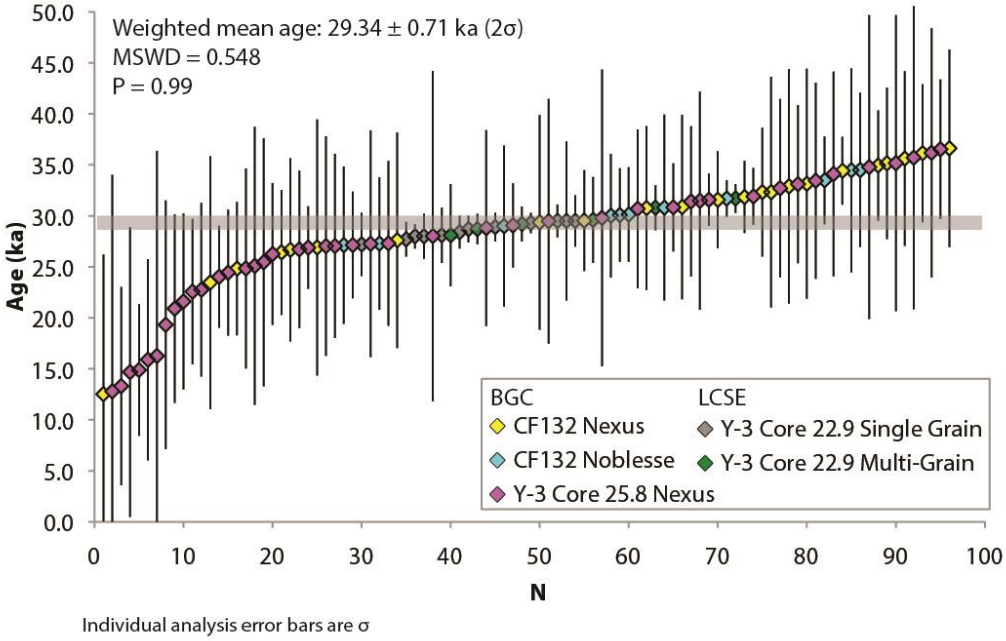

Figure S7: Rank order diagram combining all age determinations used to produce the final integrated $^{40}Ar/^{39}Ar$ weighted mean age of the Masseria del Monte Tuff.

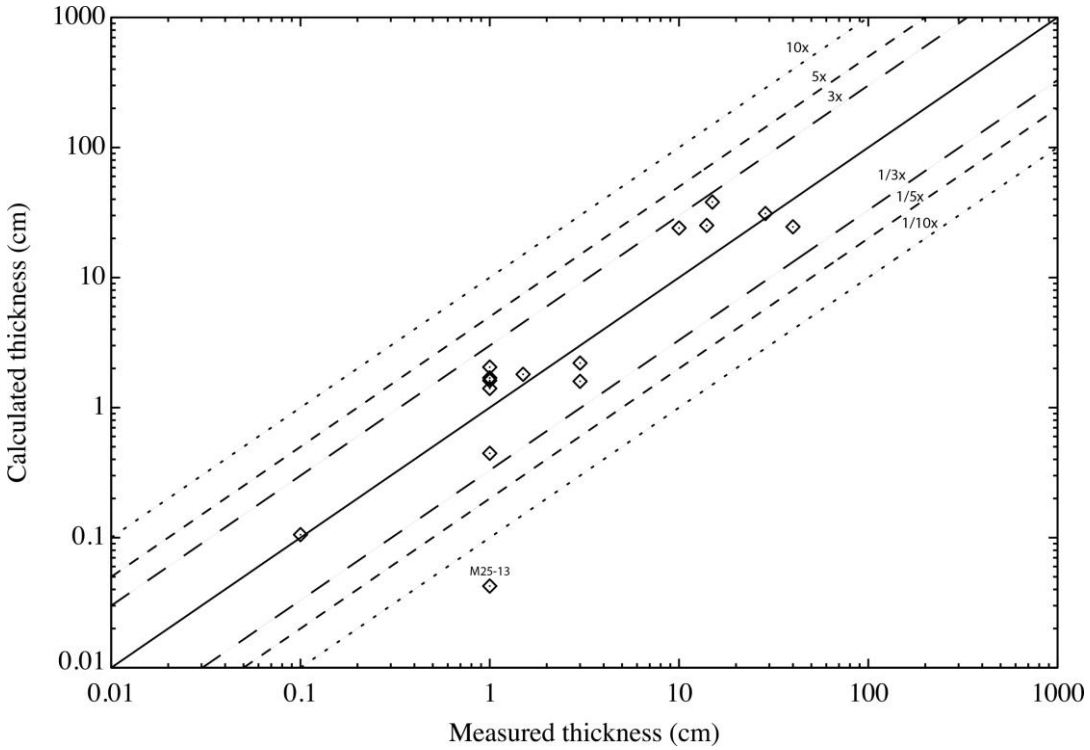

Figure S8: Comparison between the HAZMAP simulation of the Y-3 ash dispersal across the Central and Eastern Mediterranean using values obtained by best-fit procedures of tephra thickness at each sampling point. Localities and layer thickness incorporated into the HAZMAP model are presented in Supplementary Table 3, along with the explored eruption parameters in Supplementary Table 4. The equiline (black solid line) represents the ideal fit if perfect agreement can be achieved, most points lie in the region between 3 and 1/3 times.

Supplementary References

Aida, I. (1978). Reliability of a tsunami source model derived from fault parameters. *J. Phys. Earth* 26, 57–73

Albert, P.G., Hardiman, M., Keller, J, Tomlinson, E.L., Bourne, A, J., Smith, V.C. Wulf, S., Zanchetta, G., Sulpizio, R., Müller, U.C., Pross, J., Ottolini, L., Matthews, I.P., Blockley, S.P., Menzies, M.A., 2015, The Y-3 tephrostratigraphic marker revisited: new diagnostic glass geochemistry, improved chronology and climatostratigraphic interpretations: Quaternary Science Reviews, 118, 105-121.

Bonasia, R., Macedonio, G., Costa, A., Mele, D., Sulpizio, R., 2010, Numerical inversion and analysis of tephra fallout deposits from the 472 AD sub-Plinian eruption at Vesuvius (Italy) through a new best-fit procedure: Journal of Volcanology and Geothermal Research 189, 238-246.

Bourne, A.J., Lowe, J.J., Trincardi, F., Asioli, A., Blockley, S.P.E., Wulf, S., Matthews, I.P., Piva, A., Vigliotti, L., 2010, Distal tephra record for the last ca 105,000 years from core PRAD 1-2 in the central Adriatic Sea: implications for marine tephrostratigraphy: Quaternary Science Reviews 29, 3079-3094.

Buccheri, G., Bertoldo, G., Coppa, M.G., Munno, R., Pennetta, M., Siani, G., Valente, A., Vecchione, C., 2002a. Studio multidisciplinare della successione sedimentaria tardo-quaternaria proveniente dalla scarpata continentale del Golfo di Policastro (Tirreno meridionale): Boll. Soc. Geol. It. 121, 187-210.

Calanchi, N., Dinelli, E., 2008, Tephrostratigraphy of the last 170 ka in sedimentary successions from the Adriatic Sea: Journal of Volcanology and Geothermal Research 177(1), 81-95.

Calanchi, N., Cattaneo, A., Dinelli, E., Gasparottoa, G., Lucchini, F., 1998. Tephra layers in Late Quaternary sediments of the central Adriatic Sea: Marine Geology 149 (1-4),191-209.

Connor, L. & Connor, C. Inversion is the Key to Dispersion: Understanding Eruption Dynamics by Inverting Tephra Fallout. *In: Statistics in Volcanology* (Special Publications of IAVCEI, 1. Geological Society, London, pp. 231–242, 2006).

Caron, B., Sulpizio, R., Zanchetta, G., Siani, G., Santacroce, R., 2010, The Late Holocene to Pleistocene tephrostratigraphic record of Lake Ohrid (Albania): Comptes Rendus Geoscience Volume 342, 6, 453-466.

Cornell, W., Carey, S., Sigurdsson, H., 1983. Computer simulation of transport and deposition of the Campanian Y-5 ash. Journal of Volcanology and Geothermal Research 17, 89-109.

Costa, A., Dell'Erba, F., Di Vito, M.A., Isaia, R., Macedonio, G., Orsi, G., Pfeiffer, T., 2009. Tephra fallout hazard assessment at the Campi Flegrei caldera (Italy). Bulletin of Volcanology 71 (3), 259-273.

Damaschke, M., Sulpizio, R., Zanchetta, G., Wagner, B., Böhm, A., Nowaczyk, N., Rethemeyer, J., Hilgers, A., 2013. Tephrostratigraphic studies on a sediment core from Lake Prespa in the Balkans. Climate of the Past 9, 267-287

Deino, A.L., Scott, G.R., Saylor, B., Alene, M., Angelini, J.D., Haile-Selassie, Y., 2010. 40Ar/39Ar dating, paleomagnetism, and tephrochemistry of Pliocene strata of the hominid-bearing Woraso-Mille area, west-central Afar Rift, Ethiopia. Journal of Human Evolution 58, 111-126.

Di Vito, M.A., Sulpizio, R., Zanchetta, G., D'Orazio. 2008. The late Pleistocene pyroclastic deposits of the Campanian plain: New insights into the explosive activity of the Neapolitan volcanoes. Journal of Volcanology and Geothermal Research 177 (1), 19-48.

Ganser, G.H., 1993. A rational approach to drag prediction of spherical and non- spherical particles. Powder Technol. 77:143–152. https://doi.org/10.1016/0032- 5910(93)80051-B.

Giaccio, B., Hajdas, I., Isaia, R., Deino, A., Nomade, S., 2017. High-precision ^{14}C dating and $^{40}Ar/^{39}Ar$ dating of the Campanian Ignimbrite (Y-5) reconciles the time-scales of climatic-cultural processes at 40 ka. Scientific Reports 7, 45940. doi:10.1038/srep45940

Giaccio, B., Niespolo, E., Pereira, A., Nomade, S., Renne, P.E., Albert, P.G., Arienzo, I., Regattieri, E., Wagner, B., Zanchetta, G., Gaeta, M., Galli, P., Mannella, G., Peronace., E., Sottili, G., Florindo, F., Leicher, N., Marra, F., Tomlinson, E.L., 2017. First integrated tephrochronological record for the last ~190 kyr from the Fucino Quaternary lacustrine succession, central Italy. Quaternary Science Reviews 158, 211-234

Jochum, K.P., Stoll, B., Herwig, K., Willbold, M., Hofmann, A.W., Amini, M., Aarburg, S., Abouchami, W., Hellebrand, E., Mocek, B., Raczek, I., Stracke, A., Alard, O., Bouman, C., Becker, S., Dücking, M., Brätz, H., Klemd, R., de Bruin, D., Canil, D., Cornell, D., de Hoog, C., Dalpé, C., Danyushevsky, L., Eisenhauer, A., Gao, Y., Snow, J.E., Groschopf, N., Günther, D., Latkoczy, C., Guillong, M., Hauri, E., Höfer, H.E., Lahaye, Y., Horz, K., Jacob, D.E., Kasemann, S.A., Kent, A.J.R., Ludwig, T., Zack, T., Mason, P.R.D., Meixner, A., Rosner, M., Misawa, K., Nash, B.P., Pfänder, J., Premo, W.R., Sun, W.D., Tiepolo, M., Vannucci, R., Vennemann, T., Wayne, D., Woodhead, J.D., 2006. MPI-DING reference glasses for in situ microanalysis: 581 New reference values for element concentrations and isotope ratios. 582

Lane, C.S., Andric, M., Cullen, V.L., Blockley, S.P.E., 2011. The occurrence of the distal Icelandic and Italian tephra in the Lateglacial of Lake Bled, Slovenia. Quaternary Science Reviews 30(9-10), 1013-1018.

Lee, J.Y., Marti, K., Severinghaus, J.P., Kawamura, K., Yoo, H.-S., Lee, J.B., Kim, J.S., 2006. A redetermination of the isotopic abundances of atmospheric Ar. Geochimica et Cosmochimica Acta 70, 4507–4512.

Leicher, N., Zanchetta, G., Sulpizio, R., Giaccio, B., Wagner, B., Nomade, S., Francke, A., and Del Carlo, P. First tephrostratigraphic results of the DEEP site record from Lake Ohrid (Macedonia and Albania). Biogeosciences 13, 2151–2178, doi:10.5194/bg-13-2151-2016.

Macedonio, G., Costa, A., Longo, A., 2005. A computer model for volcanic ash fallout and assessment of subsequent hazard. Computers and Geoscience 31, 837-845.

Macedonio, G. and Pareschi, M.T., 1991. An algorithm for the triangulation of arbitrarily distributed points: Applications to volume estimates and terrain fitting. Comput. Geosci. 17, 859-874

Marti A., Folch A., Costa A., Engwell A. (2016) Reconstructing the plinian and co-ignimbrite sources of large volcanic eruptions: a novel approach for the Campanian Ignimbrite, Sci. Rep., 6, 21220, 1-11, doi:10.1038/srep21220

Mastin, L.G., Van Eaton, A.R., Durant, A.J., 2016. Adjusting particle-size distributions to ac- count for aggregation in tephra-deposit model forecasts. Atmos. Chem. Phys. 16: 9399–9420. https://doi.org/10.5194/acp-16-9399-2016.

Matthews, N.E., Smith, V.C., Costa, A., Durant, A.J., Pyle, D.M., Pearce, N.J.G., 2012. Ultra-distal tephra deposits from super-eruptions: Examples from Toba, Indonesia and Taupo Volcanic Zone, New Zealand. Quaternary International 258, 54-79.

Munno, R., Petrosino, P., 2004. New constraints on the occurrence of Y-3 Upper Pleistocene tephra marker layer in the Tyrrhenian Sea. Il Quaternario 17, 11-20.

Munno, R., Petrosino, P., 2007. The Late Quaternary tephrostratigraphical record of the San Gregorio Magno basin (southern Italy). Journal of Quaternary Science 22 (3), 247-266.

Mele, D., Dioguardi, F., Dellino, P., Isaia, R., Sulpizio, R., Braia, G., Hazard of pyroclastic density currents at the Campi Flegrei Caldera (Southern Italy) as deduced from the combined use of facies architecture, physical modeling and statistics of the impact parameters. Journal of Volcanology and Geothermal Research 299, 35-53.

Niespolo, E.M., Rutte, D., Deino, A.L., Renne, P.R., 2017. Intercalibration and Age of the Alder Creek 40Ar/39Ar standard. Quaternary Geochronology 39, 205-213.

Nomade, S., Renne, P.R., Vogel, N., Deino, A.L., Sharp, W.D., Becker, T.A., Jaouni, A.R., Mundil, R., 2005. Alder Creek sanidine (ACs-2): A Quaternary Ar-40/Ar-39 dating standard tied to the Cobb Mountain geomagnetic event. Chemical Geology 218, 315–338.

Paterne, M., Guichard, F., Labeyrie, J. 1988. Explosive activity of the South Italian volcanoes during the past 80,000 years as determined by marine tephrochronology. Journal of Volcanology and Geothermal Research 34, 153-172.

Poret, M., Costa, A., Folch, A., and Martì, A.: Modelling tephra dispersal and ash aggregation: The 26th April 1979 eruption, La Soufrière St. Vincent, J. Volcanol. Geotherm. Res., 347, 207–220, doi:10.1016/j.jvolgeores.2017.09.012

Renne, P.R., Balco, G., Ludwig, K.R., Mundil, R., Min, K., 2011. Response to the comment by W.H. Schwarz et al. on “Joint determination of 40K decay constants and 40Ar*/40K for the Fish Canyon sanidine standard, and improved accuracy for 40Ar/39Ar geochronology” by PR Renne, et al. (2010): Geochimica et Cosmochimica Acta 75, 5097-5100.

Renne, P.R., Sprain, C.J., Richards, M.A., Self, S., Vanderkluysen, L., Pande, K., 2015. State shift in Deccan volcanism at the Cretaceous-Paleogene boundary, possibly induced by impact: Science 350, 76-78.

Schmidt, R., Van Den Bogaard, C., Merkt, J., Muller, J., 2002, A new Lateglacial chronostratigraphic tephra marker for the southern-eastern Alps: the Neapolitan Yellow Tuff (NYT) in Langsee (Austria) in the context of a regional biostratigraphy and palaeoclimate: Quaternary International 88, 45-56.

Siani, G., Sulpizio, R., Paterne, M., Sbrana, A., 2004, Tephrostratigraphy study for the last 18,000 14C years in a deep-sea sediment sequence for the South Adriatic: Quaternary Science Reviews 23 (23-24), 2485-2500,

Smith, V.C., Isaia, R., Pearce, N.J.G., 2011, Tephrostratigraphy and glass compositions of post-15 kyr Campi Flegrei eruptions: implications for eruption history and chronostratigraphic markers: Quaternary Science reviews 30, 3638-3660.

Steiger, R.H., Jäger, E., 1977. Subcommission on geochronology: Convention on the use of decay constants in geo- and cosmochronology. Earth and Planetary Science Letters 36, 3, 359-362.

Sulpizio, R., Van Welden, A., Caron, B., Zanchetta, G., 2010. The Holocene tephrostratigraphic record of Lake Shkodra (Albania and Montenegro). Journal of Quaternary Science 25, 5, 633-650.

Sulpizio, R., Zanchetta, G., Paterne, M., Siani, G. 2003. A review of tephrostratigraphy in central and southern Italy during the last 65 ka. Il Quaternario 16, 91-108.

Wulf, S., Kraml, M., Brauer, A., Keller, J., Negendank, J.F.W., 2004. Tephrochronology of the 100 ka lacustrine sediment record of Lago Grande di Monticchio (southern Italy). *Quaternary International* 122, 7–30.

Zanchetta, G., Sulpizio, R., Giaccio, B., Siani, G., Paterne, M., Wulf, S. D'Orazio, M. 2008. The Y-3 tephra: A last glacial stratigraphic marker for the central Mediterranean basin. *Journal of Volcanology and Geothermal Research* 177(1), 145-154.